Nano Energy 58 (2019) 706–714

Contents lists available at ScienceDirect

Nano Energy

journal homepage: www.elsevier.com/locate/nanoen

Full paper

Management of the crystallization in two-dimensional perovskite solar cells with enhanced efficiency within a wide temperature range and high stability

Guangbao Wu[a], Jiyu Zhou[a], Jianqi Zhang[b], Rui Meng[a], Boxin Wang[b], Baoda Xue[b], Xuanye Leng[b], Dongyang Zhang[a], Xuning Zhang[a], Shiqing Bi[a,b], Qian Zhou[a], Zhixiang Wei[b], Huiqiong Zhou[b], Yuan Zhang[a,*]

[a] School of Chemistry, Beijing Advanced Innovation Center for Biomedical Engineering, Beihang University, Beijing 100191, PR China
[b] Key Laboratory of Nanosystem and Hierachical Fabrication, CAS Center for Excellence in Nanoscience, National Center for Nanoscience and Technology, Beijing 100190, PR China

ARTICLE INFO

Keywords:
2D perovskites
High efficiency
Crystal orientation
Hot-deposition
Recombination

ABSTRACT

Control over the crystallization in quantum well Ruddlesden-Popper phase halide perovskites is vitally important for the photovoltaic performance. Through managing the molecular stacking in 2-dimentioanl $BA_2MA_3Pb_4I_{13}$ (n = 4) perovskites based on PTAA hole transporting layers, we achieve enhanced vertical crystal orientations in $BA_2MA_3Pb_4I_{13}$ polycrystalline films, leading to a champion power conversion efficiency (PCE) of 14.3% (n ≤ 4) with negligible hysteresis in PTAA based p-i-n perovskite solar cells. The enhanced PCE is ascribed to the suppression on change recombination associated with an expedited charge extraction, revealed by transient opto-electrical analyses. Benefitted from the enhanced molecular arrangement revealed by GIWAXS, efficient charge generation at low temperatures (*T*) is enabled, leading to a negative *T*-dependence of efficiency in the hot-cast device, showing a peak PCE of 15.0% at 210 K. This trend is likely correlated to the reduced potential barriers in the quantum wells with which the detrapping of photo-carriers is facilitated at smaller thermal energy. Contrastingly, the solar cells with more randomly oriented crystals are found to suffer more from these unfavorable barriers, resulting in decreased PCEs with lowered *T*. Our findings highlight the opportunity through crystallization management coupled with interface engineering to achieve high efficiency and stable 2D perovskite solar cells within a wide *T*-window.

1. Introduction

In the last decade, hybrid organic-inorganic lead halide perovskites have become highly promising photo-absorbing materials for photovoltaic devices [1–6]. Benefitted from the high absorption efficiency, tunability in energy bandgaps, high carrier mobility, and facile solution processing, the power conversion efficiency (PCE) in solar cells based on three-dimensional (3D) perovskites has experienced a skyrocketing increase, from the initial 3.8% to the current record of 23.6% [7,8]. However, an intrinsic challenge remaining in 3D perovskites is the relative poor environmental stability due to the susceptibility to moisture, oxygen, or high temperature (*T*) [9–11]. As a result, degradations in association with the α-δ phase transition are often observed in these 3D devices upon exposure to ambient atmosphere. Besides, due to the drift of organic or halogen ions, decays in the PCE are inevitable even under a complete air-sealing environment [12]. The issue of stability has become a critical obstacle for commercial photovoltaic applications with 3D perovskites. Recently emerging Ruddlesden-Popper phase perovskites with (quasi) two-dimensional (2D) structure have exhibited a supreme stability, attracting increasing attentions [13–18]. The general formula of this class of materials is described by the formula $(RNH_3)_2A_{n-1}M_nX_{3n+1}$ (n = 1, 2, 3, 4…), where RNH_3 is a large aliphatic or aromatic alkylammonium spacer cation, e.g. butylammonium (BA) or 2-phenylethylammonium (PEA), A is the monovalent organic cation, typically of $CH_3NH_3^+$ (i.e. MA^+) or $HC(NH_2)^{2+}$ (i.e. FA^+), M is a divalent metal cation, and X is a halide anion [17,19–21]. The incorporated large-size organic spacer cations not only enhance the resistance to moisture and oxygen but effectively inhibit the drift of small organic cations or halide ions in the perovskite, allowing for a supreme stability as photo-absorbers. However, in comparison to 3D perovskites, 2D alternatives are in nature of quantum wells with intrinsically higher exciton binding energies [22]. The presence of insulating organic spacers generally hinders charge carrier transport, causing elevated losses in the PCE due to radiative recombination [21].

* Corresponding author.
E-mail address: yuanzhang@buaa.edu.cn (Y. Zhang).

https://doi.org/10.1016/j.nanoen.2019.02.002
Received 3 December 2018; Received in revised form 25 January 2019; Accepted 1 February 2019
Available online 04 February 2019

Thermodynamically, these large organic cationic layers in 2D perovskites preferentially adapt to the alignment parallel to the substrate [23]. Such packing while favorable for the lateral carrier transport in planar photodiodes or field-effect transistors [24–27], imposes difficulties for the device operation of vertical solar cells in sandwich configuration. To this end, directing the crystallization toward perpendicular stacking orientation of the organic insulating layer is of key importance to increase the device performance in 2D perovskite solar cells (PSC). To date, there have been a couple of reported attempts to improve the anisotropic crystallization in Ruddlesden-Popper phase perovskites. For example, Mohite et al. have proposed a hot casting method for the preparation of $(BA)_nMA_{n-1}Pb_nI_{3n+1}$ (n = 4) films to achieve vertical alignment of butylamine (BA) spacers, leading to PCEs of 12.51% in p-i-n solar cells with PEDOT:PSS hole transporting layers (HTLs)[23]. Zhou et al. explored the crystallization kinetics in quasi 2D perovskites based on $(BA)_2(MA,FA)_3Pb_4I_{13}$ [28]. Liu et al. reported phase transition control for high performance 2D PSCs with a PCE of 12.17% [29] and later explored stable and cesium ion-doped 2D PSCs with efficiencies exceeding 13% [30]. Chen et al. explored the orientation regulation of phenylethylammonium cations in $(PEA)_2(MA)_{n-1}Pb_nI3_{n+1}$ based solar cells and an enhanced efficiency from the original 0.56% (without NH_4SCN) to 11.01% was achieved with the optimized NH_4SCN concentration at n = 5 [18]. Ning et al. reported low-dimensional Sn based perovskite solar cells with $(PEA)_2(FA)_8Sn_9I_{28}$ which exhibited a PCE of 5.94% without the requirement of further device structure engineering [13]. Recently, it was found that the preferential alignment of the organic spacer in $(BA)_nMA_{n-1}Pb_nI_{3n+1}$ base perovskites actually initiated at the solution/air interface instead of the perovskite/substrate interface, revealed by in-situ structural characterization [31]. This result may point to the insensitivity of the crystal orientation in 2D perovskites to the chosen substrates/charge transporting layer on which the perovskite is deposited. On the other hand, based on a study concerning the operation mechanism for 2D PSCs, it was shown that charge extraction in 2D solar cells critically relies on the assistance of electrical field in conjunction with thermally-activated charge detrapping to overcome the potential barriers induced by quantum wells [22]. In this context, one expects that the performance of 2D PSCs should be affected by temperature (*T*). Despite of these progresses, to date it is yet unclear on how the ordering in the stacking of organic spacers with different HTLs impacts the photovoltaic behaviors and *T*-dependent-efficiency in 2D PSCs. Answering these questions promotes our fundamental understandings on the limitations to the operation of 2D PSCs to further boost the device efficiency.

2. Results and discussion

Here, we propose the p-i-n structure of ITO/PTAA/$BA_2MA_3Pb_4I_{13}$/C_{60}/BCP/Ag to achieve high efficiency and stable quasi-2D (herein after simply called as 2D) PSCs (see Fig. 1**a** for sketched device architecture). Through managing the crystallization of $BA_2MA_3Pb_4I_{13}$ based on polymeric PTAA (poly[bis(4-phenyl) (2,4,6-trimethylphenyl) amine) [32] as a HTL coupled with the hot-deposition method, the resultant $BA_2MA_3Pb_4I_{13}$ solar cells yield an impressive PCE of 14.3% at room temperature (RT) with negligible hysteresis, so far among the highest values reported on 2D PSCs with butylamine organic cations [33–36]. X-ray diffractometry coupled with grazing incidence wide-angle X-ray scattering (GIWAXS) evidence that the $BA_2MA_3Pb_4I_{13}$ films cast on preheated PTAA HTLs have a high crystallinity at both (111) and (202) facets in association with high proportions of vertical crystal orientation and long range ordering in crystalline domains. This morphology promotes charge sweepout with enlarged photocurrents. The modified crystal orientation leads to suppressions on charge recombination with reduced traps and enhancing the carrier lifetime by 3-fold. Through examination of *T*-dependent solar cell characteristics, we found that the 2D PSC with improved molecular stacking allows for efficient charge generation with decreased *T*. As such, a negative *T*-dependence of PCE is observed, showing a peak PCE of 15% at 210 K. In contrast, the PCE of the solar cells with more randomly oriented crystals decreases at lower *T*. Afforded by the regulated crystallization with improved film quality, the 2D PSC display small degradations < 3% after 1000 h storage in dark.

PTAA has been successfully applied as HTLs for 3D perovskite solar cells [37] (chemical structure is shown in Fig. 1**b**). As seen from the energy diagram (Fig. 1b), the highest occupied molecular orbital (HOMO) of PTAA is around 5.3 eV, which when compared to PEDOT:PSS HTLs helps reduce the energetic mismatch between the anode and the valence band of perovskites to increase the open-circuit voltage (V_{oc}). In addition, the crystallinity in 3D PSCs have been successfully regulated with PTAA HTLs [38]. On this basis, we chose PTAA as a HTL for 2D $BA_2MA_3Pb_4I_{13}$ PSCs with p-i-n architecture aiming to obtain meliorated molecular stacking and result boosts of PCE.

As a background study, we first examined the incorporation of BA cations into 2D perovksites by X-ray photoelectron spectroscopy (XPS) with the results shown in Fig. S1 in the Supporting information (SI). We observe an enlarged proportion of C1s XPS peak in $BA_2MA_3Pb_4I_{13}$, with respect to the comprared 3D $CH_3NH_3PbI_3$ film. It evidences the presence of BA cations in our perovskite films. To have insights into the structural properties of $BA_2MA_3Pb_4I_{13}$ perovskites, we performed thin film XRD and the results are displayed in Fig. 1**c**. As can be seen, the perovskite film cast on PTAA with RT-deposition displays visibly lowered crystallinity, revealed by the reduced XRD peak at 14° and 28°, corresponding to the (111) and (202) facets of $BA_2MA_3Pb_4I_{13}$ crystals, respectively. The two primary XRD peaks are both higher for the film prepared by hot-spin casting, in association with a narrowed full width at half maximum (FWHM) of 0.32 deg (versus a FWHM of 0.4 deg with RT-depostion). These results confirm the enhanced crystallinity in the hot-cast perovskite film prepared on PTAA. For comparison, we also examined the XRD of $BA_2MA_3Pb_4I_{13}$ films prepared on PEDOT:PSS (see Fig. S2, SI). Similar tendencies are observed with the peak intensity comparable to that using PTAA, implying the resemblance of crystallinity. However, as will be shown, dramatical differences in the solar cell efficiency with using PTAA and PEDOT:PSS HTLs are noted and this contrast seems to suggest other factors (rather than the average crystallinity) reponsible for the ultimate PCE.

To enable a direct visualization on the crystallization from the perovskite precursor solutions initiating on the PTAA surface, we captured the color variations during the film drying process (see snapshots in Fig. S3 SI). Through applying heat to both the precursor solution and PTAA-coated substrates, the resultant perovksite film displays a faster color variation, occurring at ~4 s after spin-coating, leading to a more abrupt black phase transition, compared to that with RT-deposition (the color changes at ~10 s).

We further examined the film morphology of perovskites prepared on PTAA HTLs by scanning electron microscopy (SEM) (see Fig. S4, SI). The perovskite film with RT-deposition displays stacked layer-by-layer structures, while such feature becomes non-observable in the hot-cast film that instead shows a smoother surface. Furthermore, we found layered flakes of perovskite crystallites, providing an implication that the large cation layer could stack in the direction parallel to the substrate, which is not harmful for the verical carrier transport. To better illustrate the morphological difference, we also compared the SEM images with large scan size (see Figure. S5, SI) A more uniform and smooth surface is observed in the hot-cast perovskite film which is associated with fewer structural defects. The distinct morphology can be understood by the heat pre-applied on the PTAA substrates, leading to different degrees of saturation of perovskite precursor solutions and resultant crystallization rate. With RT-deposition, the reduced vorpor pressure may attentuate the saturation of precursor solution, retarding the crystallization of $BA_2MA_3Pb_4I_{13}$. A slow crystallization can result in the regular layered growth of two-dimensional perovskites, which is detrimental to the vertical transport of carriers in the solar cell. In

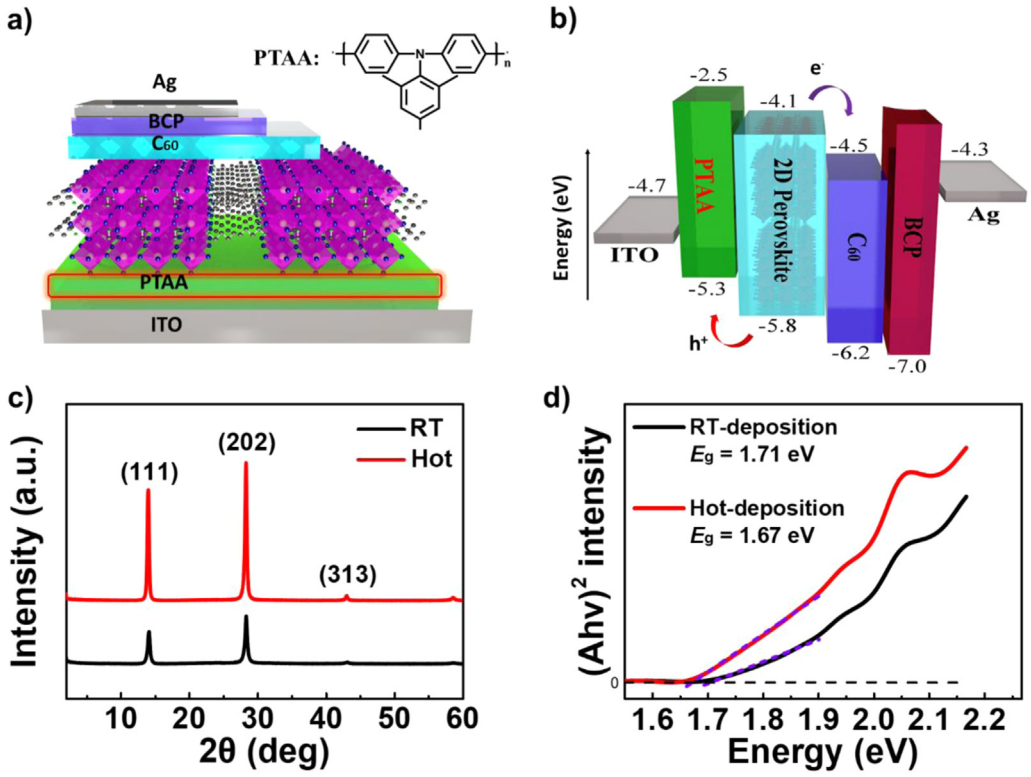

Fig. 1. (a) Planar device architecture containing the PTAA hole transporting layer (HTL) used in this study. (b) Energy diagram of 2D $BA_2MA_3Pb_4I_{13}$ alongside different charge transporting layers. (c) X-ray diffractometry of $BA_2MA_3Pb_4I_{13}$ thin films prepared on PTAA-coated substrates based on hot- and room-temperature (RT) deposition methods. (d) Tauc plot of UV-Vis-NIR absorption spectra of $BA_2MA_3Pb_4I_{13}$ thin films with different processing.

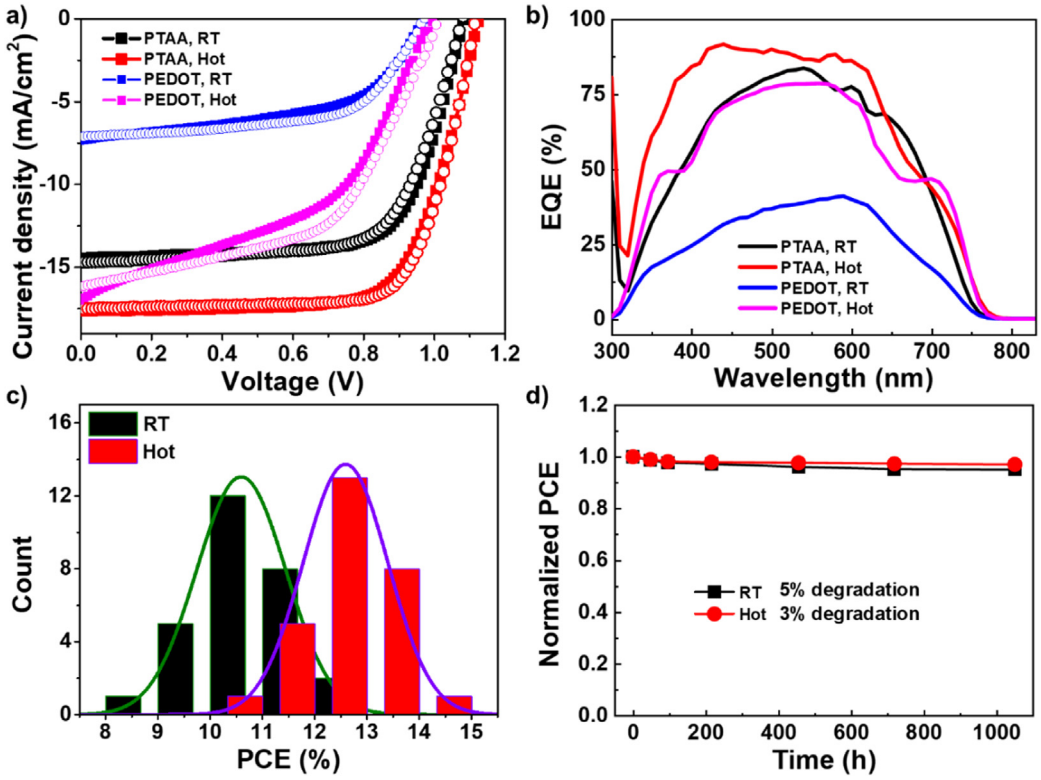

Fig. 2. (a) Current density versus voltage (*J-V*) characteristics of champion $BA_2MA_3Pb4I_{13}$ solar cells (PCE = 14.28%) with RT- and hot-deposition prepared on PTAA and PEDOT: PSS HTLs in the forward (solid symbols) and reverse (filled symbols) scan directions under AM 1.5 G solar illumination (100 mW/cm^2). (b) External quantum efficiency of according quasi-2D solar cells with different HTLs. (c) Histograpm of PCE of PTAA based $BA_2MA_3Pb4I_{13}$ solar cells obtained from 30 devices for each processing condition. (d) Normalized power conversion efficiency (PCE) of PTAA based $BA_2MA_3Pb4I_{13}$ as a function of storage time under N_2 in the dark condition.

contrast, when heat is applied, the saturation of precursor solution tends to expidite, likely resulting in a more rapid crystallization and vertical growth of large cations with enlarged grains and fewer GBs [31]. As proposed previously [39], the crystal growth style may change as a function of the saturation of perovskite precursor solutions. The fast crystallization with hot-deposition can fit to the crystal growth style model with a highly saturating precursor solution upon heating, leading to a dentritic-like growth (see illustration in Fig. S6, SI) [39], With the increasing saturaion of, for the crystallization of growth model be described by illustrated in. We further examined the surface morphology of $BA_2MA_3Pb_4I_{13}$ films with atomic force microscopy and the resultant topographic images are shown in Fig. S7 (SI). Favorably, the film with

hot-depostion is assoicated with a reduced surface roughness (RMS = 4.64 nm), compared to the RT-cast film with a larger RMS = 14.6 nm. The enhanced surface smoothness helps improve the contact properties with increased shunt resistance, beneficial for the fill factor (FF).

To confirm the dominant 2D structure in our $BA_2MA_3Pb_4I_{13}$ films, we measured the optical bandgap (E_g) with UV-Vis-NIR absorption spectroscopy (see Fig. S8, SI). Fig. 1**d** shows the Tauc plot of the absorption spectra, from which E_g was estimated. The $BA_2MA_3Pb_4I_{13}$ films with RT- and hot-deposition are associated with an E_g of 1.71 eV and 1.67 eV, respectively, consistent to the results reported in previous [23]. Similar values are obtained for the perovskites cast on PEDOT:PSS HTLs (see Fig. S7, SI). The result suggests that the bandgap of $BA_2MA_3Pb_4I_{13}$ is hardly affected by the adopted film processing in association with only a slight redshift in the absorption cutoff with hot-deposition, which is benign for the short-circuit current (J_{sc}) in solar cells. The blue shift in the 2D perovskite film with RT-deposition may be interpreted by the difference in n-value distribution [28].

With the clarified impacts of film processing and HTLs on the optical and structural properties, we turn to examine the photovoltaic performance in $BA_2MA_3Pb_4I_{13}$ 2D-PSCs. To fabricate the device, we utilized a C_{60} based electron transporting layer coupled with a BCP (2,9-dimethyl-4,7-diphenyl-1,10-phe-nanthroline) hole-blocking layer alongside the PTAA HTL. The obtained current density versus voltage (*J-V*) characteristics under standard AM 1.5 G illumination are shown in Fig. 2**a** based on the optimized film thickness (L) of 310 nm (see Fig. S9, SI). In the best case, we achieved a PCE of 14.28% with a V_{oc} of 1.11 V, a J_{sc} of 17.50 mA/cm^2 and a FF of 73.29% with hot-deposition (see device parameters summarized in Table 1). To the best of our knowledge, this value is the among the highest efficiencies reported so far on BA-containing 2D systems (n ≤ 4). In constrast, the PCE of the device with PEDOT:PSS HTL considerably reduces, due to the significant drops in the three photovoltaic parameters even with hot-deposition (see Table S1, SI). Understanding the underline mechanisms for the decreased PCE with PEDOT:PSS is beyond the main scope of the current study. While the contrasting solar cell characteristics point to the importance of utilzing PTAA HTLs in 2D PSCs to gain the PCE. Moreoever, a considerable reduction of hysteresis is noted in the champion cell, evidenced by the overlapping of *J-V* curves in the forward and reverse scans (Fig. 2a). The hysteresis index (HI) was calculated according to the relation given by [40,41],

$$\mathrm{HI} = \frac{J_{RS}(0.8V_{OC}) - J_{FS}(0.8V_{OC})}{J_{RS}(0.8V_{OC})} \quad (1)$$

The PTAA-containing device with hot-deposition exhibits the smallest HI of 0.028, which is comparable or even lower than representative high performance 3D PSCs [42–44]. The reduced hystersis can be mainly ascribed to the effective suppression on ion motions and/or surface traps in the presence of BA insulating layers, which will be discussed below. The external quantum efficiencies (EQE) of according solar cells are provided in Fig. 2**b**. The integration of EQE (PTAA, Hot:17.40 mA/cm^2) leads to small deviations < 2% with respect to the J_{sc} extracted from *J-V* characteristics, confirming the accuracy of determined device parameters. Of note, the increase of EQE for the hot-cast cell is found in a wide spectral range. Such improvement should be related to be the modified bulk properties in $BA_2MA_3Pb_4I_{13}$ with the enhanced crystallinity and crystall orientation.

Table 1
Device parameters (best) of $(BA)_2(MA)_3Pb_4I_{13}$ solar cells with PTAA HTLs based on different processing measured in the forward and reverse scan directions under AM 1.5 G solar illumination.

	Processing	V_{oc} (V)	J_{sc} (mA/cm^2)	FF (%)	PCE (%)
RT-cast	Forward	1.08	14.45	67.75	10.72
	Reverse	1.08	14.69	68.07	10.96
Hot-cast	Forward	1.12	17.60	70.31	13.92
	Reverse	1.11	17.50	73.29	14.28

The gains of photovoltaic performance with the modified crystallization are unambiguously illustrated by the histogram of PCE shown in Fig. 2**c** (based on more than 30 devices in each condition). On average, the PCE of hot-cast solar cells is boosted from 10.82% to 13.25% with the champion efficiency exceeding 14% (see Table 1). As will be evidenced, the dramatically improved PCE is mainly related to the increased anisotropy in the crystal orientation of 2D perovskite films deposited on PTAA HTLs.

Concerning the importance of stability in PSCs for realistic applications, we tracked the decay of PCEs as a function of storage time under N_2 (in dark). As shown in Fig. 2**d**, the degradation rate of PCE for the two perovskite solar cells containing PTAA HTLs exhibits a resembling fashion, likely resulting from the presence of hydrophobic BA spacer. The stability gains slightly in the device with hot-processing, leading to smaller degradations ≤ 3% after stored for 1000 h in dark (compared to ~5% degradation in the RT-cast cell). The excellent environmental stability can be correlated to the dense and compact perovskite film with reduced GBs, which increases the resistance to water or oxygen molecules. These merits promote meaningful applications of 2D perovskites with PTAA HTLs for solar energy conversion.

In order to obtain more insights into the morphological impacts on the enhanced device performance with PTAA HTLs, next we explored the crystal orientation in $BA_2MA_3Pb4I_{13}$ films by GIWAXS. Figs. 3**a** and 3**b** display 2D GIWAXS patterns of RT- and hot-cast $BA_2MA_3Pb_4I_{13}$ films. Without applying heat on the ITO/PTAA substrates, we observe a series of Debye-Scherrer diffraction rings in the film, indicative of a more isotropic distribution of scattering intensities (see Fig. 3a). This phenomenon points to more randomly orientated grains inside the polycrystalline $BA_2MA_3Pb_4I_{13}$ film. In contrast, these diffraction rings become non-observable in the hot-cast film and instead sharp and discrete Bragg spots appear along the same rings (Fig. 3b). The GIWAXS feature is suggestive of the anisotropic crystal orientation in solid films. We attempted to extract more information on the stacking orientations for the (111) and (202) facets. As compared in Figs. 3**c** and 3**d**, the (111) crystal facet stacking orientation with hot-depostion is associated with the scattering peaks at both 0 degree and 90 degree directions, and the peak asigned to the ($\bar{2}$02) stacking orientation only occurs at 0 degree. This phenomenon points to an important fact that the orientation of (202) crystal facets should be parallel to the substrate [21]. Regarding the RT-coated film, a contrast result is found that that the scattering peaks appear in any azimuths, which likely originates from the more randomly orientated grains in the polycrystalline film [31].

To assess the ordering in the stacking of crystallographic planes, we further calculated the crystal correlation length (CCL) by using the following relation [45,46],

$$CCL = \frac{2\Pi K}{\Delta q} \quad (2)$$

where Π is the ratio of circumference to diameter, K is a constant (here a value of 0.9 is used), and Δq is the half width at half-maximum of the diffraction peak. As shown in Fig. 3**e**, the (111) diffraction peak at 1 Å^{-1} for the hot-cast film presents an out-of-plane (OOP) CCL of 5.54 nm and an in-plane (IP) CCL of 5.60 nm. In comparison, the CCL in the RT-cast film amounts to 5.23 nm and 5.95 nm in the OOP and IP direction, respectively (see Fig. 3**f**). The increased CCL along OOP direction together with the reduced CCL in the IP direction strongly indicates that the crystals in $BA_2MA_3Pb_4I_{13}$ deposited on pre-heated PTAA predominantly adapt to the vertical orientation. In general, such favorable vertical stacking of BA insulating layers should prompt carrier transport and eventual collection in solar cells [47], Combining the results of GIWAXS, we illustrated a model diagram for the hot-cast $BA_2MA_3Pb4I_{13}$ film in Fig. 3**g** by highlighting that the crystalline domains are mainly oriented with their (202) crystallographic facets parallel to the substrate. This molecular orientation is one of the key

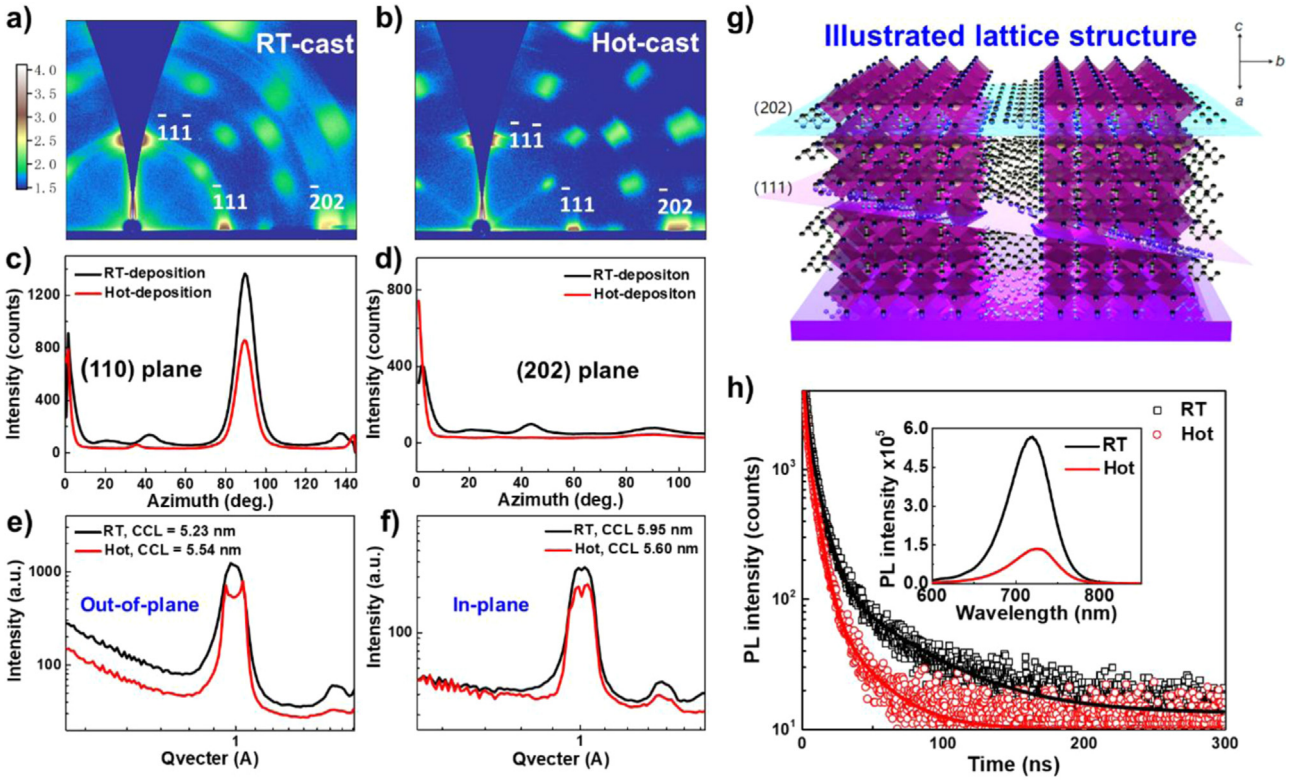

Fig. 3. (a), (b) 2D grazing incidence wide-angle X-ray scattering (GIWAXS) measured on $(BA)_2(MA)_3Pb_4I_{13}$ films processed with RT- and hot-deposition. Azimuth integral curve of $(BA)_2(MA)_3Pb_4I_{13}$ at (c) (111), and (d) (202) facets. (e), (f) Line-cut profile curves of 2D GIWAXS along out-of-plane (e) and in-plane (f) directions for the stacking of (111) plane. Also shown are calcualted crystal correlation lengths (CCL) for respective stacking orientations. (g) Model diagram of a hot-cast $(BA)_2(MA)_3Pb_4I_{13}$ perovskite film together with illustrations of respective diffraction planes. (h) Time-resolved and steady-state (inset) photoluminescence (PL) spectroscopy of $(BA)_2(MA)_3Pb_4I_{13}$ films prepared on PTAA/ITO substrates with difference deposition methods.

characteristics for achieving satisfactory device performance based on 2D perovskites.

To probe the influence of the enhanced crystal orientation on the traps and interfacial charge recombination, we employed steady-state photoluminescence (PL) spectroscopy. As shown in Fig. 3**h** Inset, a stronger quenching of PL in steady-state was observed on the sample of $BA_2MA_3Pb_4I_{13}$/PTAA with hot-deposition. This phenomenon can be explained by the facilitated hole transfer from the $BA_2MA_3Pb_4I_{13}$ photoabsorber to the PTAA HTL upon excitation. Because the same PTAA layer was used, the boosted hole transfer should be mainly related to the mitigated charge trapping either in the bulk or surface region, enabling more efficient interfacial charge (hole) transfer. As an affirmation, we performed time-resolved PL (TRPL) decay kinetics with the results shown in Fig. 3h. The TRPL traces display a three-exponential decay profile, based on which the average PL lifetime was estimted to be 13.1 ns (RT-cast film) and 6.8 ns (hot-cast film), respectively. The faster decay in PL in the presence of HTL is in line with the general picture of facilitated hole transfer, which benefits the increase of FF with reduced interfacial charge recombination [30], The mitigated recombination also can be correlated to the decreased number of voids and GBs with hot-deposition. As a result, the loss in photo-carriers via recombination is favorably descended, which reconciles the enlarged J_{sc} and PCE. The changes in the phase distribution with hot-deposition is further revealed by the steady-state PL spectra of 2D perovskite films prepared on quartz substrates with the light incident on the top surface (see Fig. S10, SI). As shown, an emission around 615 nm is observed in the RT-cast film, arising from the n = 2 phase in 2D perovskites [28]. In contrast, the PL of hot-cast film displays a single-peak feature without showing notable emissions from other minor phases in the higher energy regime. In addition, the primary PL in the host-cast film red-shifts to ~740 nm. Likely arising from n > 4 perovskites. This result provides a notion that the enhanced molecular arrangement in $BA_2MA_3Pb_4I_{13}$ films may be associated with a more uniform gradient distribution (n: $1 \rightarrow \infty$ from bottom to top).

In light of the modified recombination due to reduced charge trapping, the ideality factor (IF) in solar cells is expected to change. In this regard, we determined the IF of solar cells under irradiation by means of light intensity (P_{light})-dependent V_{oc} analysis [48]. Fig. 4**a** shows V_{oc} of PTAA containing perovskite solar cells as a function of P_{light}. As known, if the slope of V_{oc} vs. P_{light} plot equals $2kT/q$ with IF being 2 (here k is the Boltzmann constant, T is the absolute temperature and q is the elementary charge), the 1st order SRH recombination involving traps plays a significant role [48]. When the slope reduces to kT/q with IF = 1, it means that the 2nd order bi-molecular recombination dominates [49]. In our case, the extracted slopes amount to $1.82kT/q$ and $1.26kT/q$ for the devices containing RT- and hot-deposited $BA_2MA_3Pb_4I_{13}$ films, respectively. The reduced IF alongside the PL results confirms the mitigation of charge trapping through control of the crystal orientation in $BA_2MA_3Pb_4I_{13}$ perovskites.

Next, we quantitatively assessed the density of traps (N_{trap}) in our perovskite solar cells by dark carrier transport characteristics. As shown in Fig. 4**b**, the linear behavior at low bias can be related to the ohmic current in the presence of background charges [50]. With increased bias, the linear current transits to the trap-filling current (TLC), fingerprinted by the strong voltage dependence [51]. Upon further increase of the bias, a quadratic voltage dependence appears, commonly described by the space-charge limited current. Based on the voltage (V_{tr}) at which the transition from the linear transport to TLC occurs, we determined the N_{trap} with the relation given by [50],

$$N_{trap} = \frac{2\varepsilon_0\varepsilon_r V_{tr}}{qL^2} \quad (3)$$

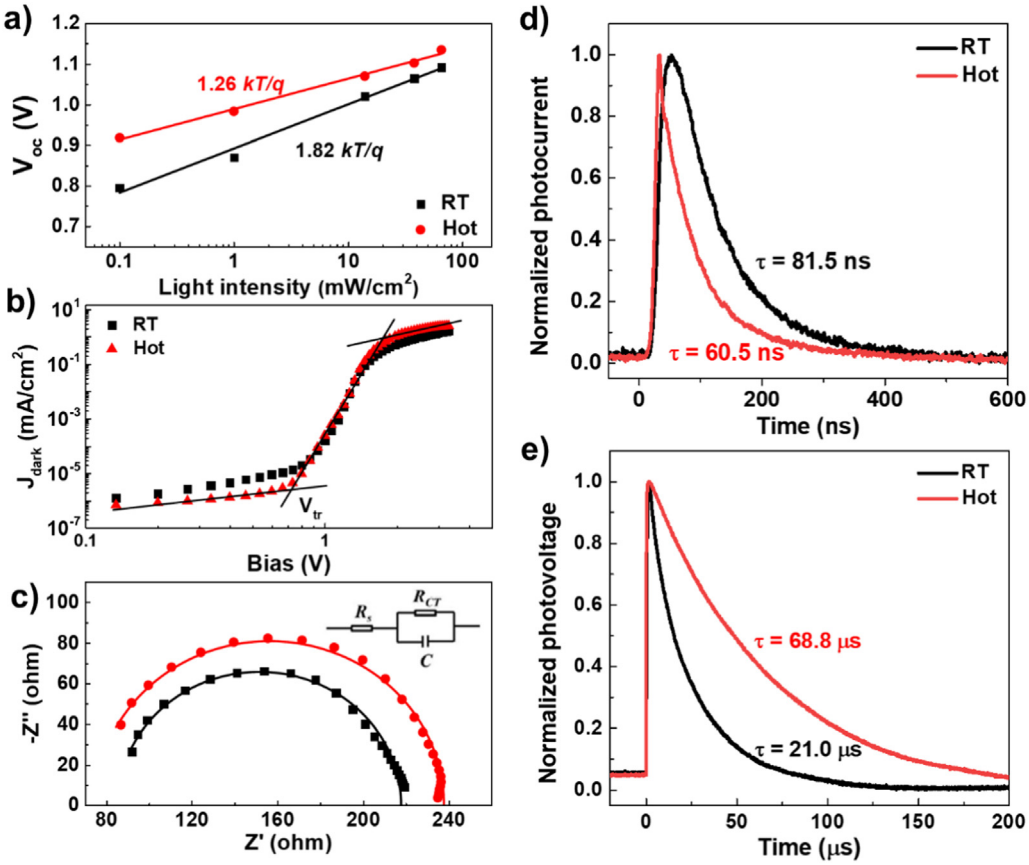

Fig. 4. (a) V_{oc} versus light intensity characteristics of PTAA-containing $BA_2MA_3Pb_4I_{13}$ solar cells with different processing. (b) Dark *J-V* characteristics of $BA_2MA_3Pb_4I_{13}$ solar cells with different processing methodss. Lines are to the guide for the eye to depict the transition from the ohmic current at lower bias to the trap-filling current. (c) Nyquist plot of impedance spectroscopy (symbols) of $(BA)_2(MA)_3Pb_4I_{13}$ solar cells measured under 1 sun (V_{oc} condition) alongside fitting results (lines) with the equivalent circuit model shown in the Inset. (d), (e) Transient photocurrent (d) and transient photovoltage (e) decays measured on RT- and hot-cast solar cells.

where ε_0 is the vacuum dielectric constant, ε_r is the relative dielectric constant of perovskites (~25), q the elemental charge and L the thickness of the active layer. The determined N_{trap} is 4.18×10^{12} cm^{-3} for the device prepared by RT-deposition and reduces to 2.16×10^{12} cm^{-3} with hot-deposition. This result is fully consistent to the decreased SRH recombination, which helps increase of the number of mobile charges upon irradation, such that the J_{sc} enlarges.

To further probe charge transport and contact properties in the solar cell operational condition, we exploited electrical impedance spectroscopy (EIS). Fig. 4**c** shows Nyquist plots of the impedance spectra measured under 1 sun irradiation (bias = V_{oc}). Based on equivalent circuit modeling (see Inset of Fig. 4c), the series resistance (R_s) dictated by the interfacial contact was determined to be 85.4 Ω (RT-cast device) and 79.4 Ω (hot-cast device). The smaller R_s can be well correlated to the promoted charge extraction with mitigated interfacial charge recombination. On the other hand, we observe an increased recombination resistance (R_{rec}) in the hot-cast device (R_{rec} = 237.9 Ω and 217.8 Ω, for hot-cast and RT-cast cells, respectively). The larger R_{rec} can be interpreted by the reduced defects related to GBs or/and foreign impurities in the hot-cast perovskite film, leading to a retardation on charge recombination.

The distinct recombination kinetics modulated by the molecular stacking in 2D perovskites are directly explored by TPC and TPC measurements with the results shown in Figs. 4**d** and 4**e**, repectively. The hot-cast device exhibits a more efficient charge sweepout with a shortened charge extraction time (τ_{ext}) from 81.5 ns (RT-cast) to 60.5 ns (hot-cast) at short-circuit condition. This phenomenon can be ascribed to the increased crystal orientation and carrier transport along to the direction of the applied electrical field. We further determined the carrier lifetime (τ_{rec}) with TPV measurements performed at open-circuit condition (Fig. 4e). Based on a mono-exponential decay model, a three-fold enhancement of τ_{rec} was identified in the device with hot-casting, agreeing to the results of EIS. Based on previous studies, the ratio of τ_{ext} to τ_{rec} has been found relevant to the FF in solar cells [52]. Upon establishing an equillibrium between charge extraction and recombination, reducing the ratio of τ_{ext} to τ_{rec} enables to shift the equillibrium toward the former process, leading to higher FFs in the device. On this basis, the enlargement of FF in the hot-cast device should result from the modulation on the two physical processes in a way that the sweepout of photo-carriers expediates and recombination retards. As a comprison, we also performed TPV/TPC measurements on a hot-cast 2D solar cell with the PEDOT:PSS HTL. From the result shown in Fig. S11, SI, a slower charge sweepout along with reduced recombination lifetime is observed. This result implies that charge extraction in the PEDOT:PSS based device tends to be impeded, causing unfavorably enhanved surface recombination. In addition to the shallower work function of PEDOT:PSS (compared to PTAA), such behavior may be caused by the non-optimized surface properties in PEDOT:PSS (with the lacking of passivation capability). Based on this rationale, the inferior PCE shown in Fig. 2a can be (partically) explained.

We also note that the V_{oc} losses (ΔV_{oc}) are slightly reduced in the PTAA containing solar cell with hot-deposition. For the champion cell with hot-deposition, the V_{oc} by is 30 meV lower than that of the RT-cast device while the E_g is ~40 mV narrower. The supressed ΔV_{oc} can be primarily related to the mitigated radiative recombination [22], leading to lowering the ΔV_{oc} around 0.57 V (compared to the ΔV_{oc} around 0.6 V with RT-depostion). Physically, the V_{oc} is governed by the splitting of quasi-Fermi levels in the photo-absorber upon irradiation, a function of charge carrier density [53], The mitigated photo-carrier losses via charge recombination can strengthen the Fermi level splitting under irradiation, with which the V_{oc} gains. Further reduction of ΔV_{oc} may resort to seek effective surface passivation to reduce nonradiative losses that constitute an important part of the total voltage losses in solar cells [22].

At last, we explored *T*-dependent photovoltaic parameters based on these 2D perovskite photo-absorbers to clarify the impact of molecular

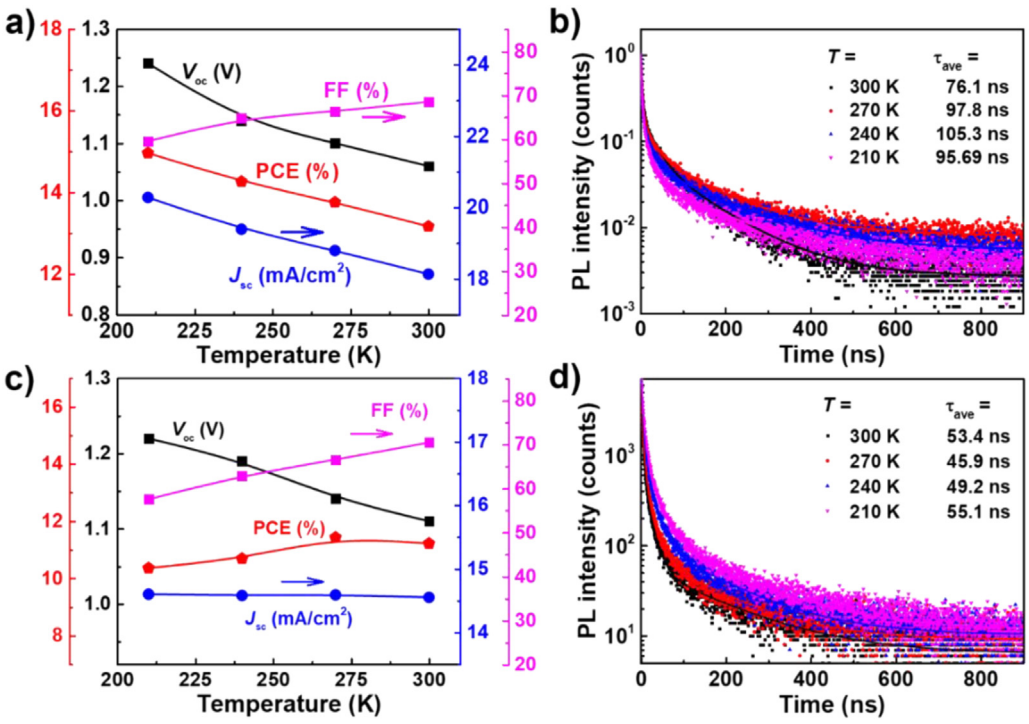

Fig. 5. (a), (c) Temperature (*T*)-dependent device parameters of $BA_2MA_3Pb_4I_{13}$ PSCs prepared by (a) hot- and (b) RT-deposition under AM 1.5G solar irradiation. (b), (d) PL decay kinetics of hot-cast (b) and RT- cast (d) $BA_2MA_3Pb_4I_{13}$ thin films measured at different *T*. Also shown in the text is the averaged PL decay time obtained from a tri-exponential decay model.

orentation on the thermally-assisted device operation. Fig. S12 (SI) shows solar cell *J-V* characteristics measured at different *T* based on a hot-cast film with the PTAA HTL. The extracted device parameters are plotted against *T* in Fig. 5**a**. Expectedly, the V_{oc} is associated with a negative *T*-coefficient, due to the *T*-dependent Fermi level splitting [22]. It is interesting to note that the J_{sc} displays a monotonic increase with decreased *T* as well in our concerned *T*-range (210–300 K), reaching 20.28 mA/cm^2 at 210 K, while the FF reduces non-substantially from 68.54% (300 K) to 59.53% (210 K). The negative *T*-dependence of J_{sc} has been observed in 3D perovskite solar cells [54,55]. while is not often observed in 2D systems. To understand this interesting phenomenon, we performed *T*-dependent PL decay measurements based on the same perovskite films coated on glass substrates (see results in Fig. 5**b**). By doing so, the influence of charge transfer can be excluded, which simplifies our analysis. We observed an incremental change in the averaged PL lifetime with the reduction of *T*, down to 240 K (see text in Fig. 5b). We further assessed the carrier mobility (here the electron mobility was examined) with single-carrier device measurements. As shown by the *J-V* characteristics in Fig. S13, SI, the electron current density in the space-charge limited regime nearly overlaps for the measurements at 300 K and 210 K. The extracted electron mobility is 4.1×10^{-4} cm^2/Vs (300 K) and 4.0×10^{-4} cm^2/Vs (210 K). Combining the results of PL and mobility, the exciton diffusion length upon irradiation tends to become longer at reduced thermal energy. This feature in general benefits the charge generation and sweepout [56]. Another attribute to the enlarged J_{sc} is manifested by the *T*-dependent PL in steady-state (Fig. S14, SI). As shown, a slight red-shift in the PL emission is observed with reduced *T*. This points to the weak bandgap narrowing which helps increase the absorbed photon density and resultant photocurrent in the solar cell. The negative *T*-dependence of J_{sc} seems to suggest that charge extraction may not be a limiting factor in 2D PSCs when the electrical field is high.

As for the dropped FF at low *T*, we can exclude the contact properties at the PTAA/ITO interface as the main limiting factor, because of the non-observable S-shape photocurrent [57]. Actually, the FF in 2D devices can be subject to the competition of electrical field-dependent charge extraction and recombination, given the presence of potential barriers [58]. At smaller fields and lower *T*, charge extraction in quantum well 2D perovskites tends to be more difficult in competition with recombination, leading to a stronger field-dependence of photocurrent, especially near the built-in potential (or flat-band condition). This rationalization reconciles the reduced in FF.

Benefitting from the enlarged J_{sc} and V_{oc} at lower *T*, the resultant PCE displays a negative *T*-dependence, showing a peak PCE of 15.0% at 210 K. This result is in contrast to a recent study on 2D PSCs containing PEDOT:PSS HTLs where visible reductions in J_{sc} and PCE with *T* were observed, due to the difficulty of charge detrapping and charge extraction at smaller thermal energies [22]. In this regard, the utilization of PTAA HTLs coupled with hot-deposition is more advantageous for the operation of 2D devices at low-*T* regime. Furthermore, in a previous study based on 3D perovskites, reduced charge trapping has been identified [59], which may be borrowed to explain the behavior of *T*-dependent photocurrent in our 2D PSCs as well.

For comparison, we also examined the photovoltaic bahaviors in the $BA_2MA_3Pb_4I_{13}$ solar cell prepared with RT-deposition. As shown by the results in Fig. 5**c** and Fig. S15, SI, a flat response of J_{sc} to *T* is observed with the FF dropping more significantly, compared to the trend in the hot-cast device. This phemonmen is in line with the *T*-dependent PL decay kinetics shown in Fig. 5**d** (based on the same perovksite film used for solar cells), in which the averaged PL lifetime for the RT-cast film is nearly unchanged at different *T*. The spectroscopic feature seems to indicate an unchanged or even reduced exciton diffusion length (if the mobiltiy decreases with *T*). Opposite to the *T*-dependence of PCE in the hot-cast device, the PCE with RT-deposition exhibits a positive *T*-coefficient in the range between 210 and 300 K. The reduced PCE with *T* is in accordance with the generally accepted fact that charge detrapping in the quantum well 2D perovskite tends to be harder with reduced thermal energy [22]. As shown recently, charge extraction in $BA_2MA_3Pb_4I_{13}$ solar cells relies on the assistance of electrical fields, due to the present potential barriers. In our case, the more efficient charge generation and extraction with hot-deposition are likely connected to the reduced potential barriers, benefitting from the long-range ordering in vertical stacking [22], These results highlight the significance of managing the crystal orientation with appropriate interface engineering to attain stable photovoltaic performance at low *T* regime.

3. Conclusion

To summarize, we demonstrate the possibility to realize high efficiency and stable 2D $BA_2MA_3Pb_4I_{13}$ perovskite solar cells through control of the crystallization on PTAA based HTLs, leading to a champion PCE of ~14.3% ($n \leq 4$) at RT. The improved photovoltaic performance is mainly attributed to the enhanced vertical crystal orientation as well as the modified charge extraction at the perovskite/PTAA interface, leading to favorable reductions in charge trapping and resultant recombination losses. With these modifications, efficient charge sweepout at short-circuit condition and elongated carrier lifetime at open-circuit condition are enabled in the $BA_2MA_3Pb_4I_{13}$ solar cell with which J_{sc} and FF are enhanced. Benefitted from the formed highly dense and smooth perovskite films, the resultant device exhibits a supreme stability with maintaining > 97% of the initial performance after > 1000 h storage in dark. Of importance, we found that the 2D device with meliorated molecular orientation can produce higher efficiencies at lower *T*, reaching a peak PCE of 15.0% at 210 K. This interesting observation is in concert with the *T*-dependent PL decay kinetics, likely attributed to the long-range ordering in vertical stacking inside the perovskite film, helpful for the reduction of potential barriers in the quantum wells. Our results illustrate a viable route afforded by management on the crystallization and interface properties to realize stable and efficient 2D perovskite solar cells within a wide *T*-window.

4. Experimental section

Experimental section is available from the Supporting Information.

Acknowledgements

This work was supported by the National Natural Science Foundation of China, (NSFC) (No. 21875012 and 21674006). Y. Z. thanks the “111” Project. H. Zhou thanks the financial support from the National Natural Science Foundation of China (NSFC) (No. 21773045), the National Key Research and Development Program of China (2017YFA0206600), and the Chinese Academy of Sciences (100 Top Young Scientists Program).

Appendix A. Supporting information

Supplementary data associated with this article can be found in the online version at doi:10.1016/j.nanoen.2019.02.002.

References

[1] A. Mei, X. Li, L. Liu, Z. Ku, T. Liu, Y. Rong, M. Xu, M. Hu, J. Chen, Y. Yang, M. Grätzel, H. Han, Science 345 (2014) 295.
[2] J. You, L. Meng, T.-B. Song, T.-F. Guo, Y. Yang, W.-H. Chang, Z. Hong, H. Chen, H. Zhou, Q. Chen, Y. Liu, N. De Marco, Y. Yang, Nat. Nanotechnol. 11 (2015) 75.
[3] H. Zhu, Y. Fu, F. Meng, X. Wu, Z. Gong, Q. Ding, M.V. Gustafsson, M.T. Trinh, S. Jin, X.Y. Zhu, Nat. Mater. 14 (2015) 636.
[4] J. Li, S.G. Bade, X. Shan, Z. Yu, Adv. Mater. 27 (2015) 5196.
[5] D. Li, H.C. Cheng, Y. Wang, Z. Zhao, G. Wang, H. Wu, Q. He, Y. Huang, X. Duan, Adv. Mater. 29 (4) (2017).
[6] J.-P. Correa-Baena, A. Abate, M. Saliba, W. Tress, T. Jesper Jacobsson, M. Grätzel, A. Hagfeldt, Energy Environ. Sci. 10 (2017) 710.
[7] A. Kojima, K. Teshima, Y. Shirai, T. Miyasaka, J. Am. Chem. Soc. 131 (2009) 6050.
[8] Y. Yang, J. You, L. Meng, Efficient and stable perovskite solar cells with all solution processed metal oxide transporting layers, US20180033983[P], 2018.
[9] G. Niu, X. Guo, L. Wang, J. Mater. Chem. A 3 (2015) 8970.
[10] M. Saliba, T. Matsui, J.Y. Seo, K. Domanski, J.P. Correa-Baena, M.K. Nazeeruddin, S.M. Zakeeruddin, W. Tress, A. Abate, A. Hagfeldt, M. Gratzel, Energy Environ. Sci. 9 (2016) 1989.
[11] T. Leijtens, G.E. Eperon, N.K. Noel, S.N. Habisreutinger, A. Petrozza, H.J. Snaith, Adv. Energy Mater. 5 (2015) 1500963.
[12] J.M. Azpiroz, E. Mosconi, J. Bisquert, F. De Angelis, Energy Environ. Sci. 8 (2015) 2118.
[13] Y. Liao, H. Liu, W. Zhou, D. Yang, Y. Shang, Z. Shi, B. Li, X. Jiang, L. Zhang, L.N. Quan, R. Quintero-Bermudez, B.R. Sutherland, Q. Mi, E.H. Sargent, Z. Ning, J. Am. Chem. Soc. 139 (2017) 6693.
[14] D.S. Lee, J.S. Yun, J. Kim, A.M. Soufiani, S. Chen, Y. Cho, X. Deng, J. Seidel, S. Lim, S. Huang, A.W.Y. Ho-Baillie, ACS Energy Lett. 3 (2018) 647.
[15] D.H. Cao, C.C. Stoumpos, T. Yokoyama, J.L. Logsdon, T.-B. Song, O.K. Farha, M.R. Wasielewski, J.T. Hupp, M.G. Kanatzidis, ACS Energy Lett. 2 (2017) 982.
[16] M. Safdari, P.H. Svensson, M.T. Hoang, I. Oh, L. Kloo, J.M. Gardner, J. Mater. Chem. A 4 (2016) 15638.
[17] N. Li, Z. Zhu, C.-C. Chueh, H. Liu, B. Peng, A. Petrone, X. Li, L. Wang, A.K.Y. Jen, Adv. Energy Mater. 7 (2017) 1601307.
[18] X. Zhang, G. Wu, W. Fu, M. Qin, W. Yang, J. Yan, Z. Zhang, X. Lu, H. Chen, Adv. Energy Mater. 8 (2018) 1702498.
[19] D.H. Cao, C.C. Stoumpos, O.K. Farha, J.T. Hupp, M.G. Kanatzidis, J. Am. Chem. Soc. 137 (2015) 7843.
[20] J.-F. Liao, H.-S. Rao, B.-X. Chen, D.-B. Kuang, C.-Y. Su, J. Mater. Chem. A 5 (2017) 2066.
[21] I.C. Smith, E.T. Hoke, D. Solis-Ibarra, M.D. McGehee, H.I. Karunadasa, Angew. Chem. Int. Ed. 53 (2014) 11232.
[22] H. Tsai, R. Asadpour, J.C. Blancon, C.C. Stoumpos, J. Even, P.M. Ajayan, M.G. Kanatzidis, M.A. Alam, A.D. Mohite, W. Nie, Nat. Commun. 9 (2018) 2130.
[23] H. Tsai, W. Nie, J.C. Blancon, C.C. Stoumpos, R. Asadpour, B. Harutyunyan, A.J. Neukirch, R. Verduzco, J.J. Crochet, S. Tretiak, L. Pedesseau, J. Even, M.A. Alam, G. Gupta, J. Lou, P.M. Ajayan, M.J. Bedzyk, M.G. Kanatzidis, Nature 536 (2016) 312.
[24] M. Yuan, L.N. Quan, R. Comin, G. Walters, R. Sabatini, O. Voznyy, S. Hoogland, Y. Zhao, E.M. Beauregard, P. Kanjanaboos, Z. Lu, D.H. Kim, E.H. Sargent, Nat. Nanotechnol. 11 (2016) 872.
[25] D. Liang, Y. Peng, Y. Fu, M.J. Shearer, J. Zhang, J. Zhai, Y. Zhang, R.J. Hamers, T.L. Andrew, S. Jin, ACS Nano 10 (2016) 6897.
[26] H. Hu, T. Salim, B. Chen, Y.M. Lam, Sci. Rep. 6 (2016) 33546.
[27] T. Matsushima, S. Hwang, A.S. Sandanayaka, C. Qin, S. Terakawa, T. Fujihara, M. Yahiro, C. Adachi, Adv. Mater. 28 (2016) 10275.
[28] N. Zhou, Y. Shen, L. Li, S. Tan, N. Liu, G. Zheng, Q. Chen, H. Zhou, J. Mater. Chem. A 140 (2018) 459.
[29] X. Zhang, R. Munir, Z. Xu, Y. Liu, H. Tsai, W. Nie, J. Li, T. Niu, D.M. Smilgies, M.G. Kanatzidis, A.D. Mohite, K. Zhao, A. Amassian, S.F. Liu, Adv. Mater. 30 (2018) 1707166.
[30] X. Zhang, X. Ren, B. Liu, R. Munir, X. Zhu, D. Yang, J. Li, Y. Liu, D.-M. Smilgies, R. Li, Z. Yang, T. Niu, X. Wang, A. Amassian, K. Zhao, S. Liu, Energy Environ. Sci. 10 (2017) 2095.
[31] A.Z. Chen, M. Shiu, J.H. Ma, M.R. Alpert, D. Zhang, B.J. Foley, D.M. Smilgies, S.H. Lee, J.J. Choi, Nat. Commun. 9 (2018) 1336.
[32] H. Chen, F. Ye, W. Tang, J. He, M. Yin, Y. Wang, F. Xie, E. Bi, X. Yang, M. Gratzel, L. Han, Nature 550 (2017) 92.
[33] W. Fu, J. Wang, L. Zuo, K. Gao, F. Liu, D.S. Ginger, A.K.Y. Jen, ACS Energy Lett. (2018) 2086.
[34] Y. Liao, H. Liu, W. Zhou, D. Yang, Y. Shang, Z. Shi, B. Li, X. Jiang, L. Zhang, L.N. Quan, R. Quintero-Bermudez, B.R. Sutherland, Q. Mi, E.H. Sargent, Z. Ning, J. Am. Chem. Soc. 139 (2017) 6693.
[35] J.-F. Liao, H.-S. Rao, B.-X. Chen, D.-B. Kuang, C.-Y. Su, J. Mater. Chem. A 5 (2017) 2066.
[36] R. Hamaguchi, M. Yoshizawa-Fujita, T. Miyasaka, H. Kunugita, K. Ema, Y. Takeoka, M. Rikukawa, Chem. Commun. 53 (2017) 4366.
[37] Q. Wang, C. Bi, J. Huang, Nano Energy 15 (2015) 275.
[38] J.H. Heo, S.H. Im, J.H. Noh, T.N. Mandal, C.-S. Lim, J.A. Chang, Y.H. Lee, H.-j. Kim, A. Sarkar, M.K. Nazeeruddin, M. Grätzel, S.I. Seok, Nat. Photon. 7 (2013) 486.
[39] H. Chen, F. Ye, W. Tang, J. He, M. Yin, Y. Wang, F. Xie, E. Bi, X. Yang, M. Gratzel, L. Han, Nature 550 (2017) 7674.
[40] J. Cao, Y.-M. Liu, X. Jing, J. Yin, J. Li, B. Xu, Y.-Z. Tan, N. Zheng, J. Am. Chem. Soc. 137 (2015) 10914.
[41] S. Bi, X. Zhang, L. Qin, R. Wang, J. Zhou, X. Leng, X. Qiu, Y. Zhang, H. Zhou, Z. Tang, Chem. Eur. J. 23 (2017) 14650.
[42] H. Yu, H. Lu, F. Xie, S. Zhou, N. Zhao, Adv. Funct. Mater. 26 (2016) 1411.
[43] P. Calado, A.M. Telford, D. Bryant, X. Li, J. Nelson, B.C. O'Regan, P.R.F. Barnes, Nat. Commun. 7 (2016) 13831.
[44] J.-W. Lee, S.-G. Kim, S.-H. Bae, D.-K. Lee, O. Lin, Y. Yang, N.-G. Park, Nano Lett. 17 (2017) 4270.
[45] G. Grancini, D. Viola, M. Gandini, D. Altamura, E.A.A. Pogna, V. D'Innocenzo, I. Bargigia, C. Giannini, G. Cerullo, A. Petrozza, ACS Energy Lett. 2 (2017) 265.
[46] X. Liu, B. Xie, C. Duan, Z. Wang, B. Fan, K. Zhang, B. Lin, F.J.M. Colberts, W. Ma, R.A.J. Janssen, F. Huang, Y. Cao, J. Mater. Chem. A 6 (2018) 395.
[47] Y. Chen, Y. Sun, J. Peng, J. Tang, K. Zheng, Z. Liang, Adv. Mater. 30 (2018) 1703487.
[48] D. Yang, X. Zhou, R. Yang, Z. Yang, W. Yu, X. Wang, C. Li, S. Liu, R.P.H. Chang, Energy Environ. Sci. 9 (2016) 3071.
[49] S. You, H. Wang, S. Bi, J. Zhou, L. Qin, X. Qiu, Z. Zhao, Y. Xu, Y. Zhang, X. Shi, H. Zhou, Z. Tang, Adv. Mater. 30 (2018) 1706924.
[50] X. Zhang, S. Bi, J. Zhou, S. You, H. Zhou, Y. Zhang, Z. Tang, J. Mater. Chem. C 5 (2017) 9376.
[51] Y. Hu, E.M. Hutter, P. Rieder, I. Grill, J. Hanisch, M.F. Aygüler, A.G. Hufnagel, M. Handloser, T. Bein, A. Hartschuh, K. Tvingstedt, V. Dyakonov, A. Baumann, T.J. Savenije, M.L. Petrus, P. Docampo, Adv. Energy Mater. 8 (2018) 1703057.
[52] Q. Xue, Y. Bai, M. Liu, R. Xia, Z. Hu, Z. Chen, X.-F. Jiang, F. Huang, S. Yang, Y. Matsuo, H.-L. Yip, Y. Cao, Adv. Energy Mater. 7 (2017) 1602333.
[53] S. Ryu, J.H. Noh, N.J. Jeon, Y. Chan Kim, W.S. Yang, J. Seo, S.I. Seok, Energy Environ. Sci. 7 (2014) 2614.
[54] W.L. Leong, Z.-E. Ooi, D. Sabba, C. Yi, S.M. Zakeeruddin, M. Graetzel, J.M. Gordon, E.A. Katz, N. Mathews, Adv. Mater. 28 (2016) 2439.

[55] S. Shao, J. Liu, H.-H. Fang, L. Qiu, G.H. ten Brink, J.C. Hummelen, L.J.A. Koster, M.A. Loi, Adv. Energy Mater. 7 (2017) 1701305.
[56] L. Peng, W. Xie, C. Yang, RSC Adv. 8 (2018) 40298.
[57] Q. Xue, Y. Bai, M. Liu, R. Xia, Z. Hu, Z. Chen, X.-F. Jiang, F. Huang, S. Yang, Y. Matsuo, H.-L. Yip, Y. Cao, Adv. Energy Mater. 7 (2017) 1602333.
[58] C. Li, F. Wang, J. Xu, J. Yao, B. Zhang, C. Zhang, M. Xiao, S. Dai, Y. Li, Z.A. Tan, Nanoscale 7 (2015) 9771.
[59] Y. Wang, C. Zhu, R. Pfattner, H. Yan, L. Jin, S. Chen, F. Molina-Lopez, F. Lissel, J. Liu, N.I. Rabiah, Z. Chen, J.W. Chung, C. Linder, M.F. Toney, B. Murmann, Z. Bao, Sci. Adv. 3 (2017) e1602076.